journal of the mechanical behavior of biomedical materials 130 (2022) 105201

Contents lists available at ScienceDirect

Journal of the Mechanical Behavior of Biomedical Materials

journal homepage: www.elsevier.com/locate/jmbbm

Fracture behavior of a composite of bone and calcium sulfate/hydroxyapatite

Joeri Kok [a,*], Elin Törnquist [a], Deepak Bushan Raina [b], Sophie Le Cann [c], Vladimir Novak [d], Aurimas Širka [e], Lars Lidgren [b], Lorenzo Grassi [a], Hanna Isaksson [a,b]

[a] Department of Biomedical Engineering, Lund University, Box 118, 221 00, Lund, Sweden
[b] Department of Clinical Sciences, Orthopedics, Lund University, BMC C12, 221 84, Lund, Sweden
[c] CNRS, Univ Paris Est Creteil, Univ Gustave Eiffel, UMR 8208, MSME, F-94010 Créteil, France
[d] Swiss Light Source, Paul Scherrer Institute, Forschungsstrasse 111, 5232, Villigen, Switzerland
[e] Lithuania University of Health Science, A.Mickeviciaus ave.2, Kaunas, Lithuania

ARTICLE INFO

Keywords:
Biomaterial
Bone cement
X-ray tomography
Synchrotron
In situ loading
Bone damage

ABSTRACT

Calcium sulfate/hydroxyapatite (CaS/HA) biomaterials have been investigated for use in several orthopedic applications. However, the mechanical interactions between the composite of CaS/HA and bone at the micro-scale are still unknown. The aim of this study was to determine if and how augmentation with CaS/HA alters the fracture behavior of bone. Eleven cylinders of trabecular bone were drilled from human femoral heads and cleaned from bone marrow. Among them, five cylinders were injected with CaS/HA to generate composite specimens, while the others were kept intact. One extra specimen of pure CaS/HA was prepared. All specimens were compressed *in situ* using synchrotron X-ray tomography and imaged at ~2% strain intervals. Structural properties were calculated from the images in unloaded state and mechanical properties were determined from the load-curves. CaS/HA alone displayed the highest peak force and stiffness and the lowest strain at fracture. All composite specimens had a higher peak force than the pure bone specimens and the composite specimens had higher toughness than the pure CaS/HA specimen. Furthermore, the fracture behavior was analyzed further to characterize the local deformations. The pure bone specimens presented damage in multiple trabeculae and the CaS/HA specimen displayed sharp transition in strains, with low strain in one load step and large cracks in the next. The composite specimens deformed uniformly, with the CaS/HA preventing tissue damage and the bone preventing cracks in the CaS/HA from propagating through the specimen. In conclusion, using tomography with *in situ* loading, it was possible to show how CaS/HA can help prevent bone tissue damage before global failure.

1. Introduction

Osteoporosis annually leads to more than 8 million fractures worldwide (Hernlund et al., 2013). Additionally, failure of fixation of orthopedic implants occurs more often in patients with low bone density (Lowe et al., 2010). Prophylactic augmentation of low-density bones using a bone cement can reduce the risk of low-energy fractures, as shown for example in femoroplasty and vertebroplasty (Kok et al., 2019; Nilsson et al., 2013). Augmentation with bone cements can also be used to improve the fixation of orthopedic implants by increasing their primary and secondary stability (Nilsson et al., 2013).

Calcium sulfate/hydroxyapatite (CaS/HA) is a biomaterial that has gained interest over the past decade due to its biphasic nature. The CaS phase resorbs within 6–8 weeks, leaving the HA particles as a scaffold which allows for bone ingrowth. Thus, the biomaterial has a high osteoconductivity (Wang et al., 2016). Moreover, the CaS phase can be used for controlled delivery of drugs such as antibiotics and bio-active molecules (Raina et al., 2019a; Stravinskas et al., 2018). Today, CaS/HA is used in clinical practice, for example, in vertebroplasties, wrist osteotomies and tibial condyle fractures (Abramo et al., 2009; Hofmann et al., 2020; Nilsson et al., 2013).

Despite its wide range of applications, the mechanical behavior of

* Corresponding author.
E-mail addresses: joeri.kok@bme.lth.se (J. Kok), elin.tornquist@bme.lth.se (E. Törnquist), deepak.raina@med.lu.se (D.B. Raina), sophie.le-cann@u-pec.fr (S. Le Cann), vladimir.novak@psi.ch (V. Novak), aurimas.sirka@lsmuni.lt (A. Širka), lars.lidgren@med.lu.se (L. Lidgren), lorenzo.grassi@bme.lth.se (L. Grassi), hanna.isaksson@bme.lth.se (H. Isaksson).

https://doi.org/10.1016/j.jmbbm.2022.105201
Received 9 June 2021; Received in revised form 19 March 2022; Accepted 25 March 2022
Available online 29 March 2022

the composite of CaS/HA and bone at the microscale is largely unknown. Detailed knowledge of how bone and CaS/HA deform and how damage accumulates under loads up to global failure may aid in the understanding of the material and, subsequently, in the development of clinical applications. Recent development in imaging techniques allows for investigation of the mechanical behavior of bone and bone-biomaterial interactions at the microscale. By using synchrotron radiation micro-computed tomography (SR-μCT) during *in situ* loading of a specimen, it is possible to study the damage mechanisms of a material (Babout et al., 2003). In addition to visual identification of crack initiation and propagation, digital volume correlation (DVC) can be used to obtain internal displacements and calculate strain fields in bone (Bay et al., 1999; Dall'Ara et al., 2017; Gillard et al., 2014; Liu and Morgan, 2007; Roberts et al., 2014; Tozzi et al., 2017; Turunen et al., 2020). DVC has previously been applied to synthetic and bovine bone specimens injected with acrylic bone cement (Zhu et al., 2016). It was shown that similar accuracy and precision of strain measurements could be achieved for the bone, the bone-cement interface, and the pure cement. On whole porcine vertebrae injected with stiff acrylic cement, it was shown that damage under compression initiated outside of the cemented region (Danesi et al., 2016). These studies on composite specimens calculated strains at a resolution of 252–2200 μm, at which the strain could generally be calculated with accuracy and precision below 0.001 (Dall'Ara et al., 2017). However, this resolution is insufficient for identifying strains within individual trabeculae as they typically have a thickness of ~150 μm in the femoral head (Fazzalari and Parkinson, 1998). By decreasing the resolution to below 40 μm, a recent study demonstrated the possibility of using DVC to investigate strains within individual trabeculae in human trabecular bone specimens with accuracy and precision around 0.001 (Turunen et al., 2020). A limitation of SR-μCT is that it exposes the samples to a large radiation dose. This can be detrimental to the sample constituents, especially the collagen, and may affect the mechanical properties of the samples (Barth et al., 2010, 2011; Peña Fernández et al., 2018a). However, by limiting total exposure (e.g., the number of images and load steps, exposure time, etc.) one can stay below the limits that have been reported to induce damage, and lead to these negative effects.

The aim of the current study was to determine if and how bone augmentation with CaS/HA alters the fracture behavior of bone. The study was performed with SR-μCT and *in situ* loading of human bone specimens, CaS/HA, and the composite of the two (bone injected with CaS/HA). The high-resolution images were used to investigate crack initiation and propagation. It was investigated if DVC could be used to shed light on the damage behavior of the bone and the biphasic resorbable CaS/HA.

2. Methods

2.1. Specimen preparation

Two human femoral heads were obtained from patients receiving a total hip replacement (approved by the Kaunas Regional Committee of Ethics of Biomedical Researches, Ethical permission: BE-2-40, 2017-06-26). One femoral head (male, 54 years, BMI 22.8 kg/m^2) was cut in half in the anterior-posterior plane. The other femoral head (female, 75 years, BMI 30 kg/m^2) was cut in half in the superior-inferior plane. Eleven cylindrical trabecular bone plugs (diameter: 6 mm, height: 7.5 mm) were drilled from the sectioned femoral heads (Fig. 1A). The bone marrow was removed from all plugs by repeated cycles of soaking in a solution of 2% TWEEN 20 (Sigma-Aldrich) for 6–10 h at 4 °C, followed by cleaning using running tap water. The plugs were considered clean of bone marrow once no more marrow could be seen by eye. After removal of the marrow, the specimens were wrapped in saline-soaked gauze and stored at 4 °C until imaging (2–3 days).

Specimens were divided into two groups (1. Bone and 2. Bone + CaS/HA) based on apparent bone volume fraction (see details in next section). Each specimen in group 1 was linked to a specimen in group 2 with similar bone volume fraction. Six specimens were kept intact, and five specimens were prepared for injection with CaS/HA (Bone Void Filler, BoneSupport AB) by placing them in a two-part POM mold held together by clamps. One gram of CaS/HA (60% CaS, 40% HA) was thoroughly mixed with 0.43 ml contrast agent (iodine based non-ionic radiographic contrast agent Iohexol®) at room temperature to obtain an injectable slurry that was transferred into a 1 ml syringe using a spatula. The mixture was gradually injected on the top of the bone plug, 0.1 ml at a time. The mold was tapped manually to ensure that the paste filled the porous bone. After a setting period of 15 min, the POM mold was unclamped, and the composite of CaS/HA and bone was retrieved and stored at 4 °C until further testing. The CaS/HA was allowed to cure for at least 1 h before mechanical testing. A third group consisting of one control specimen of CaS/HA without bone was prepared using the same mold.

2.2. Synchrotron X-ray tomography imaging

Specimens were imaged in hydrated conditions at the X02DA TOMCAT beamline, Swiss Light Source, Paul Scherrer Institute, Switzerland. After imaging, the specimens were still hydrated, as confirmed through visual inspection. Images were acquired using a beam current of 400 mA and a high-speed CMOS camera (GigaFRoST (Mokso et al., 2017)) and a high-numerical aperture 4x macroscope (Bührer et al., 2019) coupled with a 150 μm LuAG:Ce scintillator, together with a set of filters (100 μm aluminum, 50 μm copper, and 50

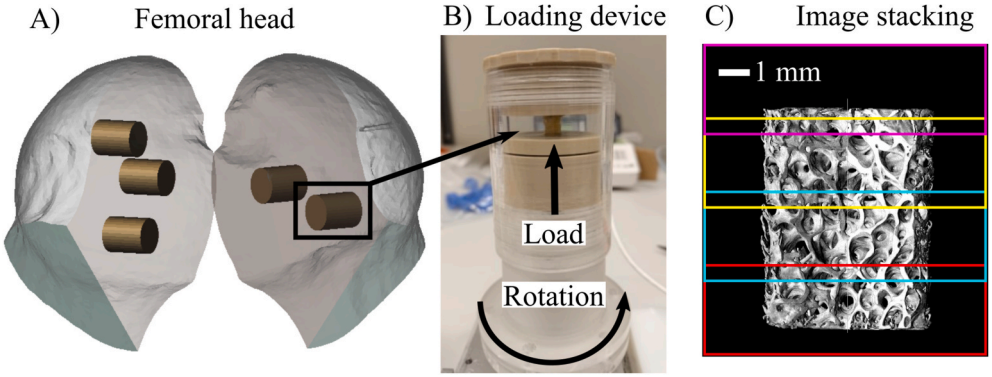

Fig. 1. A) Depiction of the size and location where the bone plugs were drilled from the femoral head. B) The loading device with a specimen in place for *in situ* loading. C) Due to vertical limitation in FOV, multiple scans were taken (indicated by the varying colors) to cover the entire specimen. (For interpretation of the references to color in this figure legend, the reader is referred to the Web version of this article.)

μm iron). With a monochromatic beam energy of 30 keV, 3000 projections were acquired over 360° rotation, using an exposure time of 6 ms, yielding an isotropic voxel size of 2.75 μm. Each scan took 18 s and covered a field-of-view (FOV) of 11 x 11 x 3 mm^3. To cover the full height of the specimen, three or four sequential scans with a slight overlap were acquired, while displacing the specimen vertically. For the division of specimens into groups, one scan of a central section of the specimen was acquired and used to estimate the bone volume/total volume (BV/TV).

For reconstruction, the projections were corrected using flat-field and dark-field images. Tomographic image volumes were reconstructed using the Gridrec algorithm with Paganin phase-retrieval (Delta: 1e-7; Beta 1.7e-10) and a Parzen filter (Marone and Stampanoni, 2012; Paganin et al., 2002) and the Sarepy algorithm for ring removal (Vo et al., 2018).

After reconstruction, each stack consisted of 1100 slices, of which approximately 200 (corresponding to 0.55 mm) overlapped with the subsequent scan. The stacks were stitched using in-house MATLAB code (Fig. 1C). The first image in the overlapping region was identified as the one providing the lowest difference in grey levels with the first image of the next stack. The stacks were then combined by calculating the average between the images of both stacks in the overlapping region.

2.3. Mechanical testing

Unconstrained uniaxial compression was performed *in situ* at a displacement rate of 0.9 mm/min (strain rate ~1.2%/min) using a custom-made loading device with a 4 kN load cell (Fig. 1B) (Le Cann et al., 2017; Turunen et al., 2020). Load steps of 0.15 mm, corresponding to approximately 2% strain, were taken until the specimen failed (3–11 load steps, whereof the first 3–4 steps were analyzed). Tomographic images were acquired before loading and after each load step. If specimens did not show a clear increase in the global stress and failure, they were excluded from further analysis. From the force-displacement curves, stress and strain were calculated. Change in height of the specimen was measured at each load step by finding matching slices of the specimen near the contact with the loading device at the top and bottom. This change in height was used to correct the strain for the compliance of the loading device and edge effects (Turunen et al., 2020). From the stress-strain curves, ultimate stress, ultimate strain, apparent modulus, and toughness were determined.

2.4. Image analysis

BV/TV of the specimens was calculated from the initial scan of the central parts before injection of the CaS/HA. The images were binarized into background and bone using a specimen-specific threshold extracted from the image histogram, defined as the valley between the two peaks corresponding to background and bone. BV/TV was determined for the imaged volume with use of BoneJ (Doube et al., 2010) (ImageJ 1.52g). After injection of the CaS/HA, specimens were imaged unloaded, to determine the CaS/HA volume/total volume (CV/TV) from the stitched volume. The images were binarized into bone-CaS/HA, and background, as bone could not be isolated from CaS/HA based on grey levels. Using BoneJ, the background volume/total volume (BgV/TV) was calculated. CV/TV was calculated as 1 – BV/TV – BgV/TV. In case the CaS/HA did not fill more than half of the void space (i.e., CV/TV < BgV/TV), the specimen was excluded from further analysis.

For each specimen, the radiation dose was estimated using an adapted simplified dose model (Lovric et al., 2013; Turunen et al., 2020). This model accounted for the image settings, specimen size, material densities, volume fractions, and absorption coefficients. The X-ray flux was measured independently with passivated, implanted planar silicon diodes (Lovric et al., 2016). For bone, a density of 1.32 g/cm^3 was assumed and a mass energy absorption coefficient of 1.07 cm^2/g was obtained from the NIST database (https://physics.nist.gov/). For CaS/HA, a density of 2.7 g/cm^3 and a mass energy absorption coefficient of 1.38 cm^2/g were assumed based on the fractions of CaS and HA, where HA was assumed to have a similar mass energy absorption coefficient as bone. In the composite specimens, the CaS/HA and bone were assumed to be perfectly mixed. Each specimen was exposed to limited additional radiation during positioning. The added dose resulting from this was estimated to remain below 3 kGy.

DVC analysis was used to visualize the displacements in the whole specimens and to identify regions where the cracks developed. Prior to DVC, a 3D median filter of ±1 voxel was applied, and the background and voids were removed using a threshold defined at the valley between the two histogram peaks corresponding to background and material. DVC analysis was carried out using the python-based DVC code TomoWarp2 (Tudisco et al., 2017). A regularly spaced grid of nodes was placed in a region of interest. In this region, TomoWarp2 calculated displacement fields by tracking sub-volumes (i.e., correlation windows) between load steps. A normalized correlation coefficient was used to find the best integer displacement, followed by sub-pixel refinement through tri-quadratic interpolation of the ±1 voxel neighborhood. Erroneous measurements following this method were corrected using a gradient-based optimization scheme to find a match for the sub-pixel displacements between the displaced and reference sub-volumes. For all load steps, displacements were calculated with respect to the unloaded specimen. After each load step, the displacements were used to obtain the new node position and to allow for cumulative calculation of displacements.

First, analysis was conducted on the entire specimen volumes, after downscaling the images four times to an isotropic voxel size of 11 μm. A correlation window of ±7 voxels and a node spacing of 7 voxels were used. Regions with sudden transitions in the displacement magnitude and relatively high strains were visually identified as regions where damage occurred. Second, longitudinal cross-sections (~7.5 x 6 x 0.3 mm) where clear damage occurred were selected for further analysis with DVC at full image resolution (voxel size of 2.75 μm). A correlation window of ±10 voxels and a node spacing of 10 voxels were used. Between each load step, the displacements were filtered with an outlier filter (if the displacement value in one voxel was more than 2 voxels higher than the median in its ±1 voxel neighborhood, it was replaced with the median of the neighborhood). There was no limit to the number of outliers that could be replaced this way. This was followed by a ±1 voxel median filter. The filtered displacements were used to calculate the maximum shear strains. The strain maps at the fourth load step (~8% global strain) were used to identify regions where damage occurred. Regions where high strains were calculated were inspected visually to confirm that these calculations were indicative of damage. The progression of damage in these regions was then inspected visually throughout all load steps.

The accuracy and precision of the strains were estimated from the unloaded images, using virtually shifted images of the volumes used for DVC (2 voxels in each orthogonal direction) and repeated scans (using the overlapping regions of the stacked scans) (Liu and Morgan, 2007). Nodes with a correlation coefficient lower than 0.95 were discarded. The accuracy and the precision were defined as the mean and standard deviation, respectively, of the average of the absolute values of the six strain components in each node (Liu and Morgan, 2007). The obtained accuracy and precision of the strains (Table 1) were considered too low to make any quantitative comparisons. Therefore, the strains were used as a proxy for identifying damaged regions.

3. Results

The specimens showed large variation in structure and CaS/HA penetration (Fig. 2). In two cases, the CaS/HA did not fill more than half of the void space. For the bone plugs, three out of the six specimens showed large deformation without a clear increase in the global stress. These five specimens were excluded from further analysis.

Table 1
Accuracy (mean) and precision (standard deviation) of the strain measurements for the three selected specimens.

		Virtually shifted		Repeated scan	
		Accuracy	Precision	Accuracy	Precision
Bone	4x downscaled	0.0052	0.0041	0.047	0.026
	Full resolution	0.0032	0.0027	0.033	0.025
CaS/HA	4x downscaled	0.0025	0.0038	0.009	0.011
	Full resolution	0.0012	0.0020	0.015	0.035
Composite	4x downscaled	0.0039	0.0042	0.017	0.017
	Full resolution	0.0016	0.0023	0.032	0.067

3.1. Mechanical testing

From the stress-strain curves, clear differences were seen between the three groups (Fig. 3 and Table 2). The ultimate stress was highest in the CaS/HA specimen, and higher for the composite specimens than for the bone specimens. The stress-strain data of the three selected specimens (highlighted in Fig. 3 and Table 2) showed that the bone and composite specimens displayed more post-yield behavior than the CaS/HA specimen, which was brittle and had a lower toughness than the composite specimens. The estimated radiation dose per scan varied from 2.0 kGy/scan for pure CaS/HA to 3.1 kGy/scan for the bone specimen with the lowest BV/TV.

3.2. Image analysis

The displacement magnitudes calculated using DVC for the downscaled images between the unloaded and the last load steps showed clear differences (Fig. 4; Supplementary Fig. 1). In the bone specimens, a steep displacement gradient was seen, indicating a concentrated region of large local deformation. In contrast, the displacements in the CaS/HA specimen displayed distinct discontinuities, originating from global failure where large cracks penetrated through the complete specimen. In the composite specimens, apart from the collapse of a void space, the displacements followed a smoother gradient. Displacements and strains for each of the first 4 load steps for each specimen presented in Fig. 4 are available in Supplementary Fig. 2.

From the refined DVC analysis, local damage was more easily observed. In the bone specimens, high local strain regions revealed trabeculae starting to bend, buckle, and crack (Fig. 5; Supplementary Fig. 1). In the CaS/HA specimen, large regions with similar displacements separated by abrupt transitions could be seen where the material failed (Fig. 6). In the presented composite specimen, three main points of interest were observed (Fig. 7). First, local collapse of a void space was observed, with microcracks in the CaS/HA surrounding the void. Second, separation between bone and CaS/HA was seen at several locations. Third, compaction of the CaS/HA was observed as a higher brightness resulting from an increased density. Displacements and strains extracted from high-resolution DVC for each of the first 4 load steps for each specimen presented in Figs. 5–7 are found in Supplementary Fig. 3, with a different highlighted region.

In regions where high strains were calculated in the bone specimens, cracking, progressive bending and/or buckling was observed throughout the loading (Fig. 8). On the contrary, progressive deformation was not observed in the CaS/HA specimen, where cracks suddenly appeared without a clear change in structure in the previous load steps (Fig. 8). The composite specimens displayed a combination of the two damage modes (Fig. 8). For these specimens, microcracks started to form and new cracks continued to form throughout the loading. Additionally, CaS/HA was found to separate from the bone at multiple locations. An accumulation of micro-damage resulted in global failure for the composite specimens.

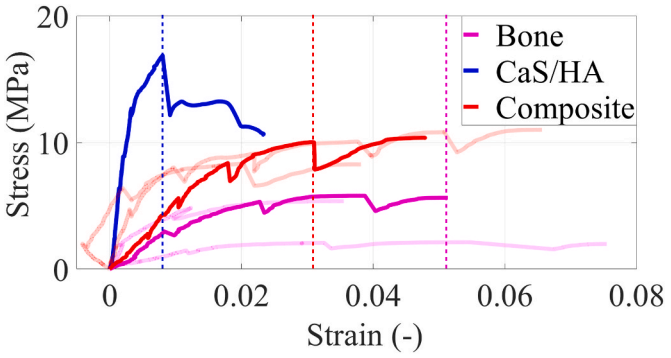

Fig. 3. Stress-strain curves for all specimen after correction for compliance and edge effects. The opaque lines represent the specimens presented in Figs. 4–8. The dotted vertical lines indicate the fourth load step for each of the selected specimens presented in Figs. 4–8.

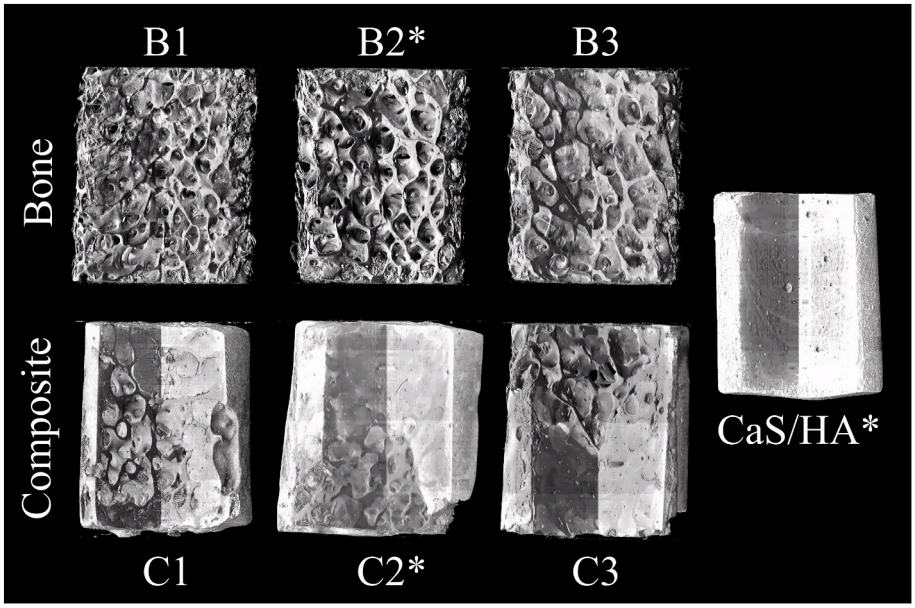

Fig. 2. Three-quarter sections of all specimens used for analysis. *Specimens presented in Figs. 4–8.

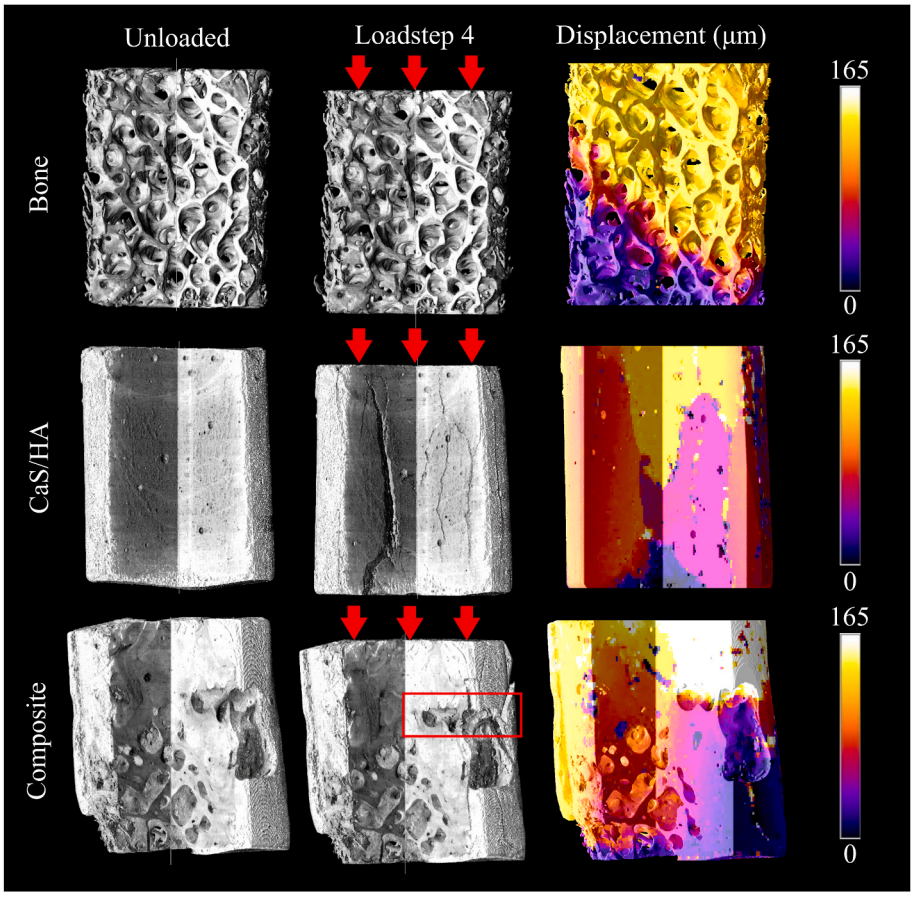

Fig. 4. Displacement magnitudes between the unloaded and the fourth load step, calculated using DVC on the 4 times downscaled image volumes of selected bone, CaS/HA, and composite specimens. The red arrows indicate the loading direction. The displacements were corrected for compliance of the device. The red box indicates the collapse of a void space in the composite specimen. All load steps and calculated shear strains are shown in Supplementary Fig. 2. Results of the remaining specimens can be found in Supplementary Fig. 1. (For interpretation of the references to color in this figure legend, the reader is referred to the Web version of this article.)

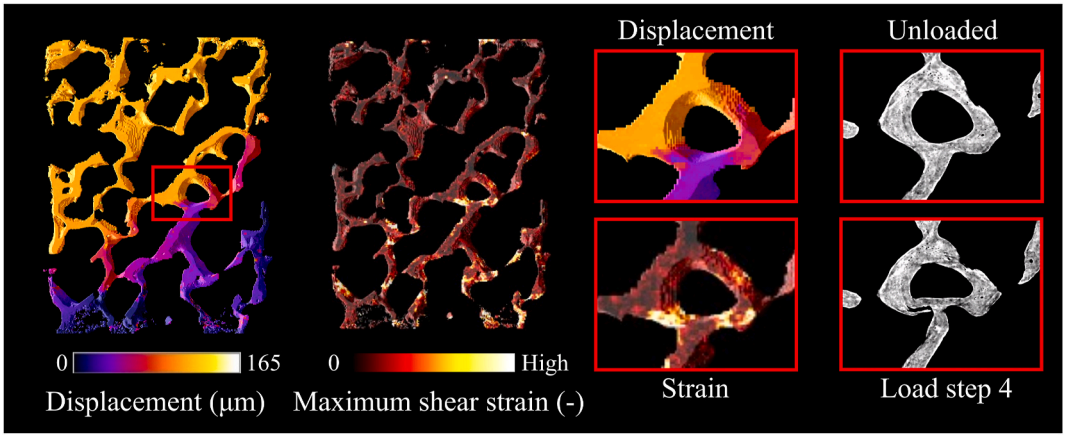

Fig. 5. Displacement magnitude and shear strains on a longitudinal cross-section at full resolution for one bone specimen. Results of the remaining specimens can be found in Supplementary Fig. 1.

4. Discussion

This study investigated how the addition of CaS/HA impacts the mechanical behavior of trabecular bone using *in situ* mechanical loading coupled with SR-μCT. The results from the mechanical loading and the local displacements and strains extracted from the images using DVC, highlighted the altered behavior of the composite. In particular, the composite specimens deformed more uniformly, with the CaS/HA preventing bone tissue damage, while the bone prevented cracks in the CaS/HA from propagating through the specimens.

Reinforcing bone with CaS/HA increased the ultimate stress, apparent modulus, and toughness. From the stress-strain curves it was clear that the composite specimens could absorb more energy than the pure bone and CaS/HA control specimens. The mechanical properties of the CaS/HA specimen were in line with those presented in other studies on CaS/HA (Nilsson et al., 2003) and on CaS-dihydrate (Koh et al., 2014). The bone specimens used for DVC analysis showed a similar ultimate stress and apparent modulus as previously presented during compression of human trabecular bone, where bone marrow was not removed and anisotropy was not accounted for (Kopperdahl and Keaveny, 1998; Morgan and Keaveny, 2001; Turunen et al., 2020).

DVC analysis of the full specimens was able to reveal differences in

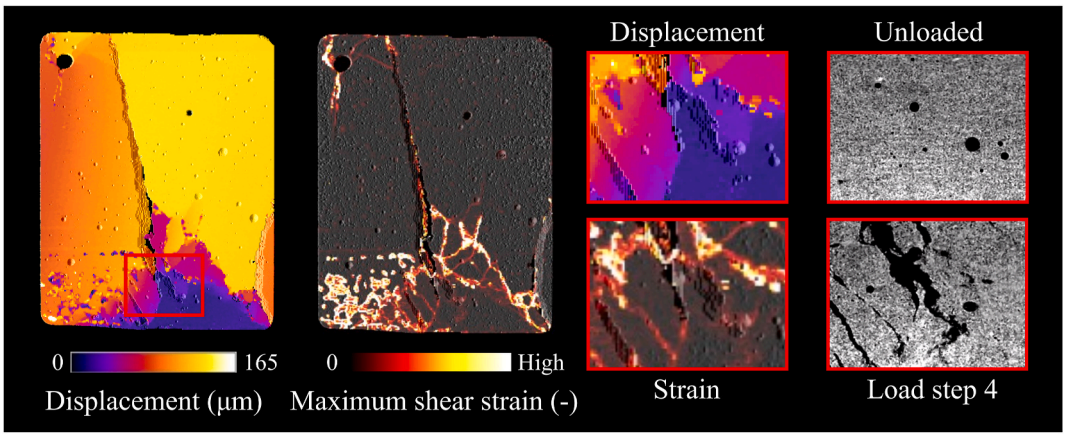

Fig. 6. Displacement magnitude and shear strain on a longitudinal cross-section at full resolution for the CaS/HA specimen.

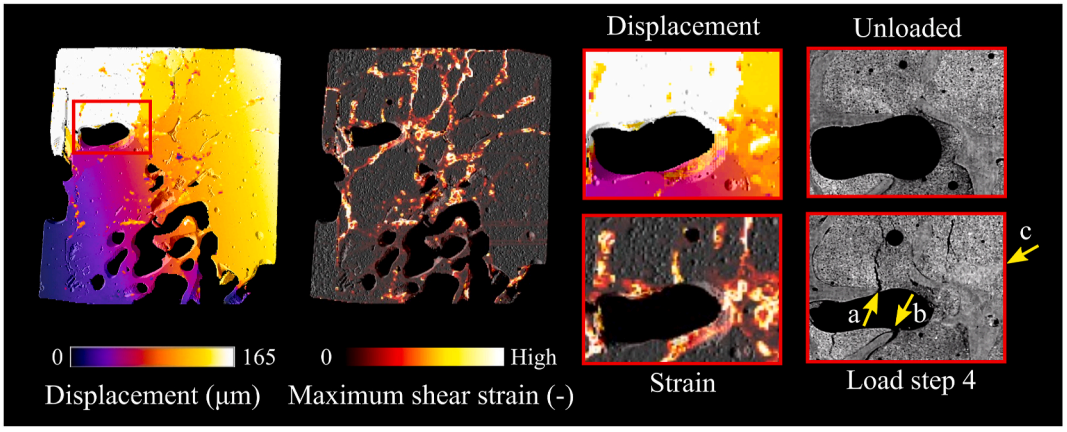

Fig. 7. Displacement magnitude and shear strain on a longitudinal cross-section at full resolution for one composite specimen. The arrows indicate three distinct modes of failure seen throughout the specimen: microcracking of the CaS/HA (a), separation between bone and CaS/HA (b), and compaction of the CaS/HA (c). Results of the remaining specimens can be found in Supplementary Fig. 1.

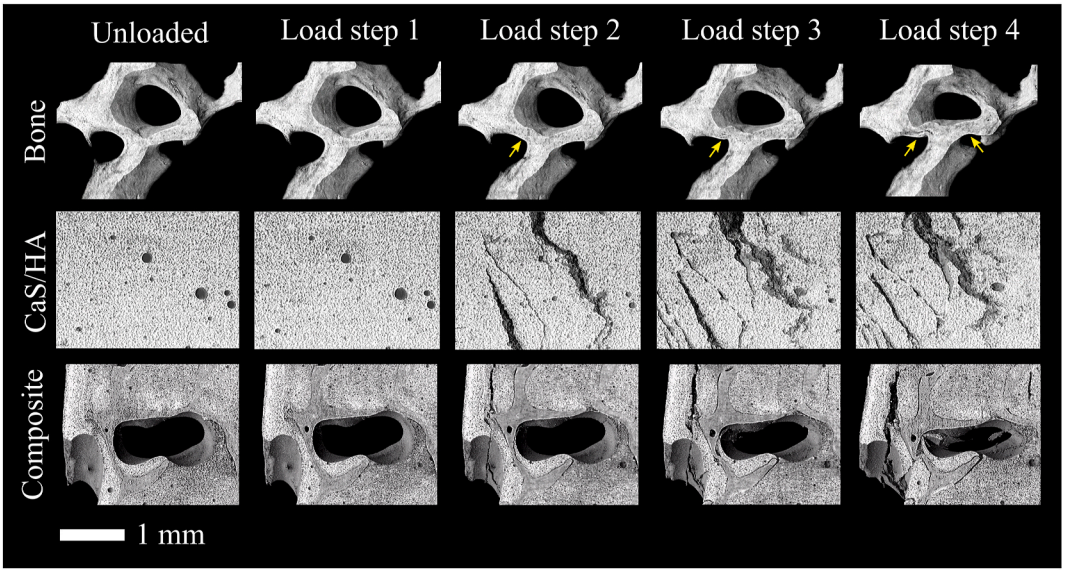

Fig. 8. Crack progression visualized in the region of interest of the selected specimens, as indicated in Figs. 5–7. Arrows in the bone specimen indicate region where progressive damage can be seen.

Table 2
Mechanical and structural properties of the specimens. *Specimens presented in Figs. 4–8.

	Bone			Composite			CaS/HA
Identifier	**B1**	**B2***	**B3**	**C1**	**C2***	**C3**	*
Ultimate stress [MPa]	2.1	5.8	5.4	11.0	10.4	8.3	16.9
Apparent modulus [Mpa]	83	238	846	897	539	776	4121
Strain at ultimate stress [-]	0.056	0.037	0.052	0.064	0.047	0.019	0.006
Toughness [J mm^{-3}]	0.13	0.24	0.15	0.60	0.33	0.34	0.28
BV/TV	0.18	0.30	0.25	0.20	0.35	0.23	–
CV/TV	–	–	–	0.48	0.57	0.40	0.99
Radiation dose [kGy/scan]	3.1	3.0	3.0	2.5	2.3	2.6	2.0

global deformation patterns between groups. The bone specimens showed large deformations, mostly within one plane due to the damage of trabeculae. The CaS/HA specimen broke up into multiple large pieces and were only held together by the applied compression. The composite specimens combined both damage mechanisms and displayed a more uniform and global deformation. These results showed that combining the mechanical characteristics of the two materials had the desired effect of absorbing higher loads and preventing tissue damage. However, due to the reduced resolution and the magnitude of errors in the displacement measurements, it was not possible to accurately calculate local strains (Supplementary Fig. 2). Strain accuracy and precision in this study ranged from 0.0012 to 0.047, and from 0.002 to 0.067, respectively (Table 1). These errors are higher than reported in comparable studies, where accuracy and precision were generally around or below 0.001 (Liu and Morgan, 2007; Turunen et al., 2020; Zhu et al., 2016). These errors were too high to allow any quantification of strains before failure. However, the main scope of the present study was to achieve the maximum spatial resolution to detect damaged regions. The strain accuracy could be increased by using a larger correlation window, but then the smaller and more local damage events can no longer be identified.

Displacements and strains were more accurately calculated in the full resolution DVC of longitudinal cross-sections. In the bone specimens, this revealed local damage in individual trabeculae. In the composite and CaS/HA specimens, damage occurred throughout the specimens. In the CaS/HA specimen, brittleness was revealed as no strains or large displacements were observed before the appearance of large cracks in the following load step (Fig. 8, Supplementary Figs. 2 and 3). For the composite specimens, DVC revealed that damage occurred throughout the specimens, and multiple damage mechanisms were identified. The combination of bone and CaS/HA lead to lower deformation within the bone itself and prevented large cracks from forming in the CaS/HA. The combination of these two mechanisms explained how the composite specimens still maintained relatively high loads at strains where the pure CaS/HA specimen failed. DVC has helped reveal the failure mechanisms of bone and CaS/HA under compressive loading. However, it is unclear if all damaged regions were identified this way, as there is currently no other standard for identifying damage from SR-μCT images of specimens loaded *in situ*.

This study has shown that CaS/HA can increase the fracture strength and amount of absorbed energy shortly after injection. This supports the use of CaS/HA to reinforce bone, during surgical interventions such as, for example, vertebroplasty. The relatively low increase in Young's modulus could also help prevent stress shielding in general, or collapse of adjacent vertebrae in the case of vertebroplasty, which is an issue sometimes occurring when bone is augmented with higher stiffness bone cements such as PMMA (Boger et al., 2007; Varga et al., 2016). The low strains at which CaS/HA fractures (compared to bone tissue) has the advantage that CaS/HA will damage first, hence more energy is absorbed before the bone is damaged. Due to this, CaS/HA could potentially be used for enhancing integration of orthopedic hardware such as nails and screws. During the late stage of osteoporosis mechanical properties of bone around a fixation device are compromised, therefore screws or nails fail to provide good initial stability, leading to failure and re-operation in up to 10–25% of patients (Augat et al., 2005; Von Rüden and Augat, 2016). After injection of CaS/HA in a patient, the CaS phase will likely resorb within several months, leaving the HA particles as a scaffold for bone ingrowth (Wang et al., 2016). This will lead to a gradual change in the local structure where the mechanical properties likely move closer to that of native bone. We also speculate that, since bone active molecules can be mixed with CaS/HA before injection (Stravinskas et al., 2018), or systemically administered postoperatively (Raina et al., 2019b), an active recruitment of osteoblasts could be achieved leading to enhanced bone formation and increased bone strength.

The calculated DVC errors were similar in bone and biomaterial (Table 1), which has also been reported in studies performed using laboratory μCT-imaging (Dall'Ara et al., 2017; Tozzi et al., 2017). However, the addition of CaS/HA reduced the contrast in the images such that fewer details in the bone phase were visible. This means that in sparse regions high strains were calculated where no damage was visually observed. These strains were left unfiltered because a high correlation coefficient was found due to the lack of detail within the correlation window. This reduced the ability to perform effective DVC analysis on the bone phase within the composite specimens. Similar errors were observed in the pure CaS/HA specimen and can be seen in the bottom-left of the displacement and strain maps in Fig. 6. The displacement step size was chosen to ensure that damage would occur from loading before reaching high radiation doses that could affect the mechanical properties (Barth et al., 2010, 2011; Peña Fernández et al., 2018b). These studies have found that exceeding a radiation dose of 35 kGy may affect the mechanical properties of trabecular bone. Dose estimations for the specimens in this study suggest that this dose limit was not reached. In most of the samples, the radiation dose was 12–17 kGy, whereas in the small regions where image volumes overlapped a double radiation dose was received, leading to a maximum total received dose of 24–34 kGy after 4 load steps. Moreover, these regions were generally not the same as those where damage progression was evaluated (Fig. 8). Additionally, a monochromatic beam was used to avoid unnecessary heat deposition on the specimens, which usually originates from lower energies. For each 18 s scan, calculations of energy absorption by the specimens in the current setup showed an estimated temperature increase of the tissue of approximately 2–4 K depending on how much heat is dissipated by the liquid. Because of aforementioned reasons, it is unlikely that any damage reported in this study is a result of radiation damage. Nevertheless, more studies should be performed to better understand the effect of the repeated SR-μCT imaging on the local microdamage in bone-cement specimens.

A limitation in this study is the limited penetration of CaS/HA in the composite specimens. This puts a restriction on the comparison of mechanical properties between groups. In a clinical setting, bone marrow is displaced by the pressure applied during insertion of CaS/HA (Kok et al., 2019). Since the bone plugs were retrieved and no longer part of a closed compartment, the bone marrow was removed to improve the penetration of CaS/HA into the bone. This may have led to a less exact representation of how the spreading would occur clinically. Due to the small spaces between the trabeculae and the relatively high viscosity and setting speed of CaS/HA, the material did not successfully fill all void space. Furthermore, it is possible that the protocol for the removal of bone marrow influenced the mechanical performance of the bone tissue. Carter and Hayes (1977) suggested that the absence of bone marrow should not affect the mechanical properties at the presented strain rate. However, their chemical method used for removal of bone marrow was

found to itself affect the mechanical properties of bone (Vesper et al., 2017). The method for bone marrow removal used in the current study was similar to those presented in other studies (Belda et al., 2020; Kasra and Grynpas, 2007; Sas et al., 2021), with the exception of the long soaking times, leaving the specimens unthawed for a few days before testing. These studies did not report any effect on the mechanical properties from this specific marrow removal process. To maximize the number of specimens retrieved, the femoral heads were cut in half and trabecular bone was drilled from both sides. Due to the limited depth left for drilling before reaching the cortex, not all specimens could be cut to exactly 7.5 mm with perfectly flat surfaces. Additionally, drilling can lead to some damage to the bone. This led to geometrical variation between specimens, and damage at the surface was identified before loading in several specimens. For some specimens this may have resulted in uneven loading and a lack of increase in global stress. This was more apparent in specimens with a low BV/TV. Variation and surface damage can be decreased by further optimizing the sample preparation protocol and consistently drilling along the main loading axis of the femoral head, accounting for anisotropy. This will also lead to higher ultimate stress and apparent modulus, generally around 20 MPa and 3 GPa respectively (Morgan and Keaveny, 2001; Sas et al., 2021).

In conclusion, this study has shown that the addition of CaS/HA can help strengthen trabecular bone and greatly increase its ability to absorb energy during deformation, keeping the bone largely intact. The use of SR-μCT and the proposed DVC has the potential of identifying regions where damage occurred on the microscale. This information supports the use of CaS/HA as a biomaterial that can be used for orthopedic implementation where reinforcement of bone or stabilization of a fixation device is required. Additionally, these findings can be used to support new clinical applications for CaS/HA.

CRediT authorship contribution statement

Joeri Kok: Writing – original draft, Visualization, Methodology, Formal analysis, Data curation, Conceptualization. **Elin Törnquist:** Writing – review & editing, Methodology, Investigation. **Deepak Bushan Raina:** Writing – review & editing, Methodology, Investigation. **Sophie Le Cann:** Writing – review & editing, Methodology, Investigation. **Vladimir Novak:** Writing – review & editing, Resources, Methodology. **Aurimas Širka:** Writing – review & editing, Resources. **Lars Lidgren:** Writing – review & editing, Resources. **Lorenzo Grassi:** Writing – review & editing, Supervision, Conceptualization. **Hanna Isaksson:** Writing – review & editing, Supervision, Funding acquisition, Conceptualization, Investigation.

Declaration of competing interest

The authors declare the following financial interests/personal relationships which may be considered as potential competing interests: Lars Lidgren reports a relationship with Bone Support AB that includes: board membership. Lars Lidgren reports a relationship with Orthocell Limited that includes: board membership.

Acknowledgements

We thank J. Engqvist and S. Hall for lending us the load cell, BoneSupport AB for the CaS/HA material, and the Paul Scherrer Institut, Villigen, Switzerland for provision of synchrotron radiation beamtime at the X02DA TOMCAT beamline. This work was supported by the Swedish Agency for Innovation Systems (VINNOVA) [grant number 2017–00269], the Swedish Research Council [grant number 2015-04795; 2019–04517], and the European Union's Horizon 2020 research and innovation program under the Marie Skłodowska-Curie grant agreement [grant number 713645].

Appendix A. Supplementary data

Supplementary data to this article can be found online at https://doi.org/10.1016/j.jmbbm.2022.105201.

References

Abramo, A., Geijer, M., Kopylov, P., Ta, M., 2009. Osteotomy of distal radius fracture malunion using a fast remodeling bone substitute consisting of calcium sulphate and calcium phosphate. J. Biomed. Mater. Res. B Appl. Biomater. 281–286. https://doi.org/10.1002/jbm.b.31524.

Augat, P., Simon, U., Liedert, A., Claes, L., 2005. Mechanics and mechano-biology of fracture healing in normal and osteoporotic bone. Osteoporos. Int. 16, 36–43. https://doi.org/10.1007/s00198-004-1728-9.

Babout, L., Ludwig, W., Maire, E., Buffi E Ere, J.Y., 2003. Damage assessment in metallic structural materials using high resolution synchrotron X-ray tomography. Nucl. Instrum. Methods Phys. Res. B 200, 303–307.

Barth, H.D., Launey, M.E., MacDowell, A.A., Ager, J.W., Ritchie, R.O., 2010. On the effect of X-ray irradiation on the deformation and fracture behavior of human cortical bone. Bone 46, 1475–1485. https://doi.org/10.1016/j.bone.2010.02.025.

Barth, H.D., Zimmermann, E.A., Schaible, E., Tang, S.Y., Alliston, T., Ritchie, R.O., 2011. Characterization of the effects of X-ray irradiation on the hierarchical structure and mechanical properties of human cortical bone. Biomaterials 32, 8892–8904. https://doi.org/10.1016/j.biomaterials.2011.08.013.

Bay, B.K., Smith, T.S., Fyhrie, D.P., Saad, M., 1999. Digital volume correlation: three-dimensional strain mapping using X-ray tomography. Exp. Mech. 39, 217–226. https://doi.org/10.1007/BF02323555.

Belda, R., Palomar, M., Peris-Serra, J.L., Vercher-Martínez, A., Giner, E., 2020. Compression failure characterization of cancellous bone combining experimental testing, digital image correlation and finite element modeling. Int. J. Mech. Sci. 165, 105213 https://doi.org/10.1016/j.ijmecsci.2019.105213.

Boger, A., Heini, P., Windolf, M., Schneider, E., 2007. Adjacent vertebral failure after vertebroplasty: a biomechanical study of low-modulus PMMA cement. Eur. Spine J. 16, 2118–2125. https://doi.org/10.1007/s00586-007-0473-0.

Bührer, M., Stampanoni, M., Rochet, X., Büchi, F., Eller, J., Marone, F., 2019. High-numerical-aperture macroscope optics for time-resolved experiments. J. Synchrotron Radiat. 26, 1161–1172. https://doi.org/10.1107/S1600577519004119.

Carter, D.R., Hayes, W.C., 1977. The compressive behavior of bone as a two-phase porous structure. J. Bone Jt. Surg. 59-A, 954–962. https://doi.org/10.1007/978-1-4471-5451-8_116.

Dall'Ara, E., Peña-Fernández, M., Palanca, M., Giorgi, M., Cristofolini, L., Tozzi, G., 2017. Precision of digital volume correlation approaches for strain analysis in bone imaged with micro-computed tomography at different dimensional levels. Front. Mater 4. https://doi.org/10.3389/fmats.2017.00031.

Danesi, V., Tozzi, G., Cristofolini, L., 2016. Application of digital volume correlation to study the efficacy of prophylactic vertebral augmentation. Clin. Biomech. 39, 14–24. https://doi.org/10.1016/j.clinbiomech.2016.07.010.

Doube, M., Kłosowski, M.M., Arganda-carreras, I., Fabrice, P., 2010. UKPMC Funders Group BoneJ : free and extensible bone image analysis in ImageJ. Bone 47, 1076–1079. https://doi.org/10.1016/j.bone.2010.08.023.BoneJ.

Fazzalari, N.L., Parkinson, I.H., 1998. Femoral trabecular bone of osteoarthritic and normal subjects in an age and sex matched group. Osteoarthritis Cartilage 6, 377–382. https://doi.org/10.1053/joca.1998.0141.

Gillard, F., Boardman, R., Mavrogordato, M., Hollis, D., Sinclair, I., Pierron, F., Browne, M., 2014. The application of digital volume correlation (DVC) to study the microstructural behaviour of trabecular bone during compression. J. Mech. Behav. Biomed. Mater. 29, 480–499. https://doi.org/10.1016/j.jmbbm.2013.09.014.

Hernlund, E., Svedbom, A., Ivergård, M., Compston, J., Cooper, C., Stenmark, J., McCloskey, E.V., Jönsson, B., Kanis, J.A., 2013. Osteoporosis in the European union: medical management, epidemiology and economic burden: a report prepared in collaboration with the international osteoporosis foundation (IOF) and the European federation of pharmaceutical industry associations (efpia). Arch. Osteoporos 8. https://doi.org/10.1007/s11657-013-0136-1.

Hofmann, A., Gorbulev, S., Guehring, T., Schulz, A.P., Schupfner, R., Raschke, M., Huber-Wagner, S., Rommens, P.M., 2020. Autologous iliac bone graft compared with biphasic hydroxyapatite and calcium sulfate cement for the treatment of bone defects in tibial plateau fractures: a prospective, randomized, open-label, multicenter study. J. Bone Joint Surg. Am. 102, 179–193. https://doi.org/10.2106/JBJS.19.00680.

Kasra, M., Grynpas, M.D., 2007. On shear properties of trabecular bone under torsional loading: effects of bone marrow and strain rate. J. Biomech. 40, 2898–2903. https://doi.org/10.1016/j.jbiomech.2007.03.008.

Koh, I., Lopez, A., Helgason, B., Ferguson, S.J., 2014. The compressive modulus and strength of saturated calcium sulphate dihydrate cements : implications for testing standards. J. Mech. Behav. Biomed. Mater. 34, 187–198. https://doi.org/10.1016/j.jmbbm.2014.01.018.

Kok, J., Širka, A., Grassi, L., Raina, D.B., Tarasevičius, Š., Tägil, M., Lidgren, L., Isaksson, H., 2019. Fracture strength of the proximal femur injected with a calcium sulfate/hydroxyapatite bone substitute. Clin. Biomech. 63 https://doi.org/10.1016/j.clinbiomech.2019.03.008.

Kopperdahl, D.L., Keaveny, T.M., 1998. Yield strain behavior of trabecular bone. J. Biomech. 31, 601–608. https://doi.org/10.1016/S0021-9290(98)00057-8.

Le Cann, S., Tudisco, E., Perdikouri, C., Belfrage, O., Kaestner, A., Hall, S., Tägil, M., Isaksson, H., 2017. Characterization of the bone-metal implant interface by Digital

Volume Correlation of in-situ loading using neutron tomography. J. Mech. Behav. Biomed. Mater. 75, 271–278. https://doi.org/10.1016/j.jmbbm.2017.07.001.
Liu, L., Morgan, E.F., 2007. Accuracy and precision of digital volume correlation in quantifying displacements and strains in trabecular bone. J. Biomech. 40, 3516–3520. https://doi.org/10.1016/j.jbiomech.2007.04.019.
Lovric, G., Barré, S.F., Schittny, J.C., Roth-Kleiner, M., Stampanoni, M., Mokso, R., 2013. Dose optimization approach to fast X-ray microtomography of the lung alveoli. J. Appl. Crystallogr. 46, 856–860. https://doi.org/10.1107/S0021889813005591.
Lovric, G., Mokso, R., Schlepütz, C.M., Stampanoni, M., 2016. A multi-purpose imaging endstation for high-resolution micrometer-scaled sub-second tomography. Phys. Med. 32, 1771–1778. https://doi.org/10.1016/j.ejmp.2016.08.012.
Lowe, J.A., Crist, B.D., Bhandari, M., Ferguson, T.A., 2010. Optimal treatment of femoral neck fractures according to patient's physiologic age: an evidence-based review. Orthop. Clin. N. Am. 41, 157–166. https://doi.org/10.1016/j.ocl.2010.01.001.
Marone, F., Stampanoni, M., 2012. Regridding reconstruction algorithm for real-time tomographic imaging. J. Synchrotron Radiat. 19, 1029–1037. https://doi.org/10.1107/S0909049512032864.
Mokso, R., Schlepütz, C.M., Theidel, G., Billich, H., Schmid, E., Celcer, T., Mikuljan, G., Sala, L., Marone, F., Schlumpf, N., Stampanoni, M., 2017. GigaFRoST: the gigabit fast readout system for tomography. J. Synchrotron Radiat. 24, 1250–1259. https://doi.org/10.1107/S1600577517013522.
Morgan, E.F., Keaveny, T.M., 2001. Dependence of yield strain of human trabecular bone on anatomic site, 34, pp. 569–577.
Nilsson, M., Wielanek, L., Wang, J.S., Tanner, K.E., Lidgren, L., 2003. Factors influencing the compressive strength of an injectable calcium sulfate-hydroxyapatite cement. J. Mater. Sci. Mater. Med. 14, 399–404. https://doi.org/10.1023/A:1023254632704.
Nilsson, M., Zheng, M.H., Tägil, M., 2013. The composite of hydroxyapatite and calcium sulphate: a review of preclinical evaluation and clinical applications. Expet Rev. Med. Dev. https://doi.org/10.1586/17434440.2013.827529.
Paganin, D., Mayo, S.C., Gureyev, T.E., Miller, P.R., Wilkins, S.W., 2002. Simultaneous phase and amplitude extraction from a single defocused image of a homogeneous object. J. Microsc. 206, 33–40. https://doi.org/10.1046/j.1365-2818.2002.01010.x.
Peña Fernández, M., Cipiccia, S., Dall'Ara, E., Bodey, A.J., Parwani, R., Pani, M., Blunn, G.W., Barber, A.H., Tozzi, G., 2018a. Effect of SR-microCT radiation on the mechanical integrity of trabecular bone using in situ mechanical testing and digital volume correlation. J. Mech. Behav. Biomed. Mater. 88, 109–119. https://doi.org/10.1016/j.jmbbm.2018.08.012.
Peña Fernández, M., Cipiccia, S., Dall'Ara, E., Bodey, A.J., Parwani, R., Pani, M., Blunn, G.W., Barber, A.H., Tozzi, G., 2018b. Effect of SR-microCT radiation on the mechanical integrity of trabecular bone using in situ mechanical testing and digital volume correlation. J. Mech. Behav. Biomed. Mater. 88, 109–119. https://doi.org/10.1016/j.jmbbm.2018.08.012.
Raina, D.B., Larsson, D., Sezgin, E.A., Isaksson, H., Tägil, M., Lidgren, L., 2019a. Biomodulation of an implant for enhanced bone-implant anchorage. Acta Biomater. 96, 619–630. https://doi.org/10.1016/j.actbio.2019.07.009.
Raina, D.B., Liu, Y., Isaksson, H., Tägil, M., Lidgren, L., 2019b. Synthetic hydroxyapatite: a recruiting platform for biologically active molecules. Acta Orthop. 91, 126–132. https://doi.org/10.1080/17453674.2019.1686865.
Roberts, B.C., Perilli, E., Reynolds, K.J., 2014. Application of the digital volume correlation technique for the measurement of displacement and strain fields in bone: a literature review. J. Biomech. 47, 923–934. https://doi.org/10.1016/j.jbiomech.2014.01.001.
Sas, A., Helgason, B., Ferguson, S.J., van Lenthe, G.H., 2021. Mechanical and morphological characterization of PMMA/bone composites in human femoral heads. J. Mech. Behav. Biomed. Mater. 115, 104247 https://doi.org/10.1016/j.jmbbm.2020.104247.
Stravinskas, M., Tarasevicius, S., Laukaitis, S., Nilsson, M., Raina, D.B., Lidgren, L., 2018. A ceramic bone substitute containing gentamicin gives good outcome in trochanteric hip fractures treated with dynamic hip screw and in revision of total hip arthroplasty : a case series. BMC Muscoskel. Disord. 8, 1–7. https://doi.org/10.1186/s12891-018-2360-8.
Tozzi, G., Dall'Ara, E., Palanca, M., Curto, M., Innocente, F., Cristofolini, L., 2017. Strain uncertainties from two digital volume correlation approaches in prophylactically augmented vertebrae: local analysis on bone and cement-bone microstructures. J. Mech. Behav. Biomed. Mater. 67, 117–126. https://doi.org/10.1016/j.jmbbm.2016.12.006.
Tudisco, E., Andò, E., Cailletaud, R., Hall, S.A., 2017. TomoWarp2: a local digital volume correlation code. Software 6, 267–270. https://doi.org/10.1016/j.softx.2017.10.002.
Turunen, M.J., Le Cann, S., Tudisco, E., Lovric, G., Patera, A., Hall, S.A., Isaksson, H., 2020. Sub-trabecular strain evolution in human trabecular bone. Sci. Rep. 10, 1–14. https://doi.org/10.1038/s41598-020-69850-x.
Varga, P., Hofmann-Fliri, L., Blauth, M., Windolf, M., 2016. Prophylactic augmentation of the osteoporotic proximal femur—mission impossible? BoneKEy Rep. 5, 7270. https://doi.org/10.1038/bonekey.2016.86.
Vesper, E.O., Hammond, M.A., Allen, M.R., Wallace, J.M., 2017. Even with rehydration, preservation in ethanol influences the mechanical properties of bone and how bone responds to experimental manipulation HHS public access. Bone 97, 49–53. https://doi.org/10.1016/j.bone.2017.01.001.
Vo, N.T., Atwood, R.C., Drakopoulos, M., 2018. Superior techniques for eliminating ring artifacts in X-ray micro-tomography. Opt Express 26, 28396. https://doi.org/10.1364/oe.26.028396.
Von Rüden, C., Augat, P., 2016. Failure of fracture fixation in osteoporotic bone. Injury 47. https://doi.org/10.1016/S0020-1383(16)47002-6. S3–S10.
Wang, J.S., Tägil, M., Isaksson, H., Boström, M., Lidgren, L., 2016. Tissue reaction and material biodegradation of a calcium sulfate/apatite biphasic bone substitute in rat muscle. J. Orthop. Transl. 6, 10–17. https://doi.org/10.1016/j.jot.2015.11.002.
Zhu, M.L., Zhang, Q.H., Lupton, C., Tong, J., 2016. Spatial resolution and measurement uncertainty of strains in bone and bone-cement interface using digital volume correlation. J. Mech. Behav. Biomed. Mater. 57, 269–279. https://doi.org/10.1016/j.jmbbm.2015.12.017.